

Journal Pre-proof

Effect of impurities on ultra-pure hydrogen production by pressure vacuum swing adsorption

Ayub Golmakani, Seyed Ali Nabavi, Vasilije Manović



PII: S1226-086X(19)30562-3
DOI: <https://doi.org/10.1016/j.jiec.2019.10.024>
Reference: JIEC 4830
To appear in: *Journal of Industrial and Engineering Chemistry*
Received Date: 29 July 2019
Revised Date: 14 September 2019
Accepted Date: 19 October 2019

Please cite this article as: Golmakani A, Nabavi SA, Manović V, Effect of impurities on ultra-pure hydrogen production by pressure vacuum swing adsorption, *Journal of Industrial and Engineering Chemistry* (2019), doi: <https://doi.org/10.1016/j.jiec.2019.10.024>

This is a PDF file of an article that has undergone enhancements after acceptance, such as the addition of a cover page and metadata, and formatting for readability, but it is not yet the definitive version of record. This version will undergo additional copyediting, typesetting and review before it is published in its final form, but we are providing this version to give early visibility of the article. Please note that, during the production process, errors may be discovered which could affect the content, and all legal disclaimers that apply to the journal pertain.

© 2019 Published by Elsevier.

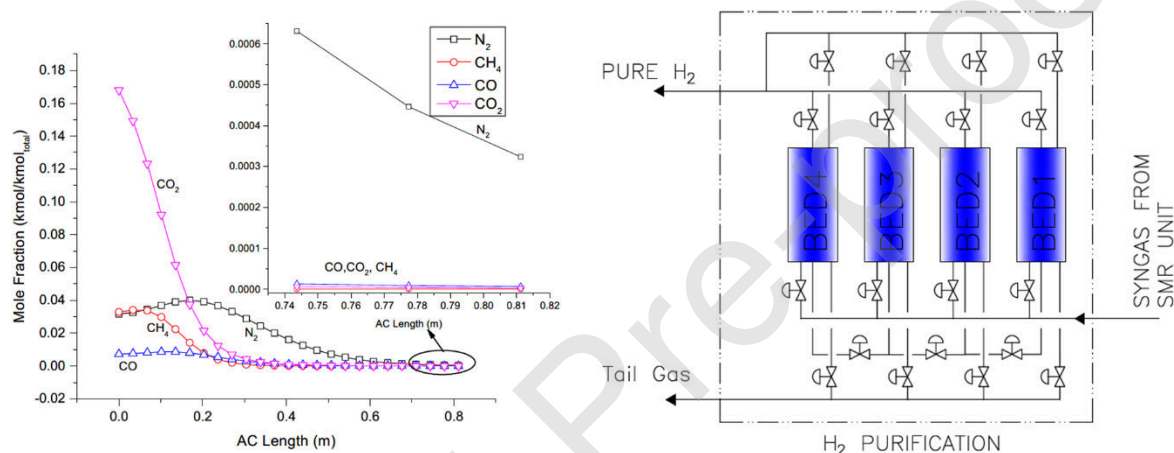
Effect of impurities on ultra-pure hydrogen production by pressure vacuum swing adsorption

Ayub Golmakani*, Seyed Ali Nabavi, Vasilije Manović

Centre for Climate and Environmental Protection, Cranfield University, Bedford,
 Bedfordshire MK43 0AL, UK

*Corresponding author: Ayub Golmakani (ayub.golmakani@cranfield.ac.uk)

Graphical abstract



Highlights:

- Effect of syngas impurities on energy consumption of PVSA process is studied
- 2% lower N₂ concentration in syngas leads to 55% reduction in energy consumption
- Development of novel adsorbents with better N₂ removal performances is required

Abstract

The most viable technology for production of ultra-pure hydrogen (>99.99%), required for fuel cells, is steam methane reforming (SMR) coupled with pressure vacuum swing adsorption (PVSA). A PVSA process with a two-layer bed of activated carbon (AC)/zeolite 5A for ultra-pure hydrogen production from syngas was developed and simulated with the aim

of exploring the effect of impurities on energy intensity of the process. The simulated concentration profiles showed that CH₄ was removed by first half of the AC layer, CO₂ and CO were mostly removed by the end of that layer, but zeolite 5A (the second layer) could not completely remove the remaining N₂. Further, the effect of the N₂ on performance of the PVSA process was demonstrated by simulating purification of two feeds with 3.1 and 1.1 vol% N₂, respectively. The 2% drop in N₂ concentration in the syngas feed resulted in decreased energy consumption of the PVSA process from 940 kJ/kg to 430 kJ/kg H₂, while H₂ recovery increased from 47% to 55%. Therefore, the presence of N₂ has a very large impact on recovery and energy intensity of the ultra-pure hydrogen production process, and development of adsorbents with better N₂ removal performances is required.

Abbreviations

AC	activated carbon
AD	adsorption
AD&PPG	adsorption and providing purge
BD	blow down
BFW	boiler feed water
CSS	cyclic steady state
E	exchanger
ED1	first equalisation depressurisation
ED2	second equalisation depressurisation
EP1	first equalisation pressurisation
EP2	second equalisation pressurisation
GHG	greenhouse gas
LDF	linear driving force
ODE	ordinary differential equation
PDE	partial differential equation
PEI	polyetherimide
PG	purge

PSA	pressure swing adsorption
PVSA	pressure vacuum swing adsorption
RP	repressurisation
SMR	steam methane reforming
TSA	temperature swing adsorption
VA	vacuum

Keywords: syngas impurities; pressure vacuum swing adsorption; fuel cell specifications; cyclic adsorption process; hydrogen production

Nomenclature:

Item	Description	Unit
a_p	specific pore surface area of adsorbent	m^2/m^3
A_w	cross sectional area of the wall	m^2
C_{COP}	CO concentration at bed outlet	$\frac{\text{mol}}{\text{m}^3}$
C_{eDT}	total gas concentration at exit of bed during de-pressurisation	$\frac{\text{mol}}{\text{m}^3}$
$C_{eD,i}$	component i, gas concentration at exit of bed during de-pressurisation	$\frac{\text{mol}}{\text{m}^3}$
$C_{feed,i}$	component i concentration in feed	$\frac{\text{mol}}{\text{m}^3}$
$C_{feed,T}$	total gas concentration in feed	$\frac{\text{mol}}{\text{m}^3}$
$C_{purge,i}$	component i concentration at bed inlet during regeneration (purge step)	$\frac{\text{mol}}{\text{m}^3}$
$C_{g,i}$	component i concentration in gas phase of bed	$\frac{\text{mol}}{\text{m}^3}$
C_{gT}	total gas concentration in gas phase of bed	$\frac{\text{mol}}{\text{m}^3}$
C_{H2f}	hydrogen concentration in feed	$\frac{\text{mol}}{\text{m}^3}$
C_{H2P}	concentration of hydrogen at bed outlet	$\frac{\text{mol}}{\text{m}^3}$

C_{ip}	concentration of component i at bed outlet	$\frac{\text{mol}}{\text{m}^3}$
C_{ps}	specific heat of adsorbent at constant pressure	$\frac{\text{J}}{\text{kg K}}$
C_{pw}	specific heat of the wall at constant pressure	$\frac{\text{J}}{\text{kg K}}$
C_p	molar specific heat at constant pressure	$\frac{\text{J}}{\text{mol K}}$
$C_{v,ads,i}$	molar specific heat of adsorbed phase of component i at constant volume	$\frac{\text{J}}{\text{mol K}}$
C_v	molar specific heat at constant volume	$\frac{\text{J}}{\text{mol K}}$
$C_{v,i}$	molar specific heat of component i at constant volume	$\frac{\text{J}}{\text{mol K}}$
D_B	diameter of bed	m
$D_{z,i}$	dispersion coefficient of component i	$\frac{\text{m}^2}{\text{s}}$
d_p	diameter of particle	m
h_f	heat transfer coefficient in gas film surrounding adsorbent particle	$\frac{\text{W}}{\text{m}^2 \text{K}}$
h_o	heat transfer coefficient between wall and ambient	$\frac{\text{W}}{\text{m}^2 \text{K}}$
h_w	heat transfer coefficient in gas film at wall	$\frac{\text{W}}{\text{m}^2 \text{K}}$
P	gas pressure	bar
$P_{atm.}$	atmospheric pressure	bar
$P_{equib.}$	equilibrium pressure of 2 connected beds	bar
P_H	pressure of bed before connecting to bed at lower pressure	bar
P_i	component i partial pressure	bar
P_L	pressure of bed before connecting to bed at higher pressure	bar
$P_{product}$	pressure at product outlet	bar
P_{sbd}	pressure at beginning of blow down	bar
P_{srp}	pressure at beginning of re-pressurisation	bar
$P_{va.}$	Pressure during vacuum step	bar

q_i	component i loading	$\frac{mol}{kg}$
q_i^*	component i equilibrium loading	$\frac{mol}{kg}$
R_{Bi}	inner diameter of column	m
R_{Bo}	outer diameter of column	m
r_p	radius of adsorbent particle	m
T_{feed}	temperature of feed	K
T_{eDT}	temperature at the outlet of bed during depressurisation	K
T_{gf}	gas temperature at bed inlet	K
T_g	gas temperature	K
T_p	temperature of sorbent particle	K
T_w	temperature of wall	K
T_∞	temperature of ambient	K
t	time	s
t_{ads}	duration of adsorption step	s
t_{cycle}	cycle time	s
t_{purge}	duration of purge step	s
$t_{repress}$	duration of re-pressurisation step	s
u_{sfeed}	superficial velocity of feed at bed inlet	$\frac{m}{s}$
u_s	superficial velocity	$\frac{m}{s}$
u_{spurge}	superficial velocity at bed inlet during regeneration (purge step)	$\frac{m}{s}$
u_{sp}	superficial velocity of product at bed outlet	$\frac{m}{s}$
u_{seD}	superficial velocity in bed during depressurisation	$\frac{m}{s}$
w_{ads}	mass of adsorbent in bed	kg
w_i	LDF coefficient	$\frac{1}{s}$
y_i	mole fraction of component i	(mol/mol)

γ	C_p/C_v ratio	(—)
ϵ	bed porosity	(—)
ϵ_p	particle porosity	(—)
ρ_p	density of adsorbent particle	$\frac{kg}{m^3}$
ρ_b	bulk density of adsorbent	$\frac{kg}{m^3}$
ρ_w	density of wall	$\frac{kg}{m^3}$
μ	gas viscosity	$\frac{kg}{ms}$
λ	coefficient of axial heat dispersion	$\frac{J}{smK}$
$(-\Delta H_{ads})_i$	component i heat of adsorption	$\frac{J}{mol}$

1. Introduction

Fossil fuel use in the transportation sector over the past century has experienced tremendous growth due to increases in the quality of life and the world economy. On the other hand, utilisation of fossil fuels in the transport sector contributed considerably to urban air pollution and now accounts for 29% of global greenhouse gas (GHG) emissions, which demands an urgent solution [1–6]. Hydrogen fuel cells have been considered as one of the best solutions for achieving zero-emission targets since the only product is water [7–10].

Several methods exist for hydrogen production, including solid oxide steam electrolysis, photoelectrochemical water splitting, electrolytic hydrogen generation, steam methane reforming (SMR), polyetherimide (PEI) membranes, and partial oxidation and thermal decomposition of fossil fuels [11–18]. Among these methods, SMR combined with pressure swing adsorption (PSA) is currently the most commercially established technology for

production of hydrogen that can meet the required specification of hydrogen fuel cells. In this method, a SMR unit produces syngas containing 70-80% H₂, 15-30% CO₂, 2-4% CH₄, 0.5-2% CO, and 1-3% N₂, which is followed by a PSA unit that removes impurities and produces ultra-pure hydrogen (>99.99% H₂, <10 ppm CO) [19,20].

Adsorbents used in PSA units should have high adsorption capacity and be capable of removing all the impurities. However, N₂ and CO removal are challenging, since conventional adsorbents have much higher affinities towards CO₂ and CH₄. Finding a single adsorbent with high removal capacity for all impurities is difficult and, usually, a multi-layer configuration of different sorbents is used in PSA units [21–25]. The commonly employed first layer in commercial PSA units is activated carbon (AC), which is used for adsorption of CO₂ and CH₄. The second layer is zeolite, used for adsorption of CO and N₂ [24]. Since zeolite cannot be regenerated at atmospheric conditions, evacuation (pressure vacuum swing adsorption, PVSA) is required [20].

Nitrogen in produced syngas originates from natural gas and, also, from the dry-seal gas of the compressors that are required during the compression of natural gas in transmission pipelines, and the compressors of the SMR unit. Zhong et al. [27] suggested using hydrogen for sealing of compressors; however, this raises the safety risk, because the dry-seal gas should be inert to prevent any potential explosion. Carbon dioxide is also an alternative for sealing of compressors that feed the hydrogen production unit of refineries, since it can be removed much more easily than nitrogen in PSA units. The syngas produced by steam reforming of ethanol is highly interesting because CH₄, CO and CO₂ are the only impurities. Abdeljaoued et al. [25] used a four-bed PSA process with 12 steps for a feed stream with 69% H₂, 25% CO₂, 5% CH₄, and 1% CO, and they produced hydrogen with 99.9913% purity,

achieving 75.5% recovery. Wei et al. [28] modelled a one-column PVSA process for syngas containing 79% H₂, 1.2% CO, 17% CO₂, 0.7% N₂, and 2.1% CH₄, and the simulations predicted hydrogen production of 99.17% purity, with a recovery of 58.94%. Xiao et al. [29] simulated a one-bed, four-step PSA cycle for a mixture of 67% H₂, 28% CO₂, and 5% N₂ and found that hydrogen with 98.249% purity at 49.8% recovery could be produced. In addition, for a mixture of 68% H₂, 27% CO₂, 5% CO, they achieved a hydrogen purity of 99.696% and a recovery of 47.75%. Shi et al. [30] designed a ten-bed PSA process with activated carbon (first layer) and zeolite 5A (second layer) for producing hydrogen with 99.99% purity and 85% recovery from syngas with a composition of 76% H₂, 20% CO₂, 3.5% CH₄ and 0.5% CO, produced in a SMR unit.

Carbon monoxide is detrimental for fuel cell performance due to blocking and consequently reducing active sites on the catalyst for hydrogen oxidation. Values as high as 100 ppm CO cause sudden and rapid failure of fuel cells, and those as low as 10 ppm can still have detrimental effects for fuel cell performance [1,31–33]. Therefore, CO concentrations below 0.2 ppm have been typically considered for assuring effective long- term performance of fuel cells [34,35]. Methane is another impurity which can also be removed by conventional adsorbents like activated carbon [36–38]. To produce hydrogen with fuel cell specifications, various cyclic adsorption methods like PSA, PVSA and temperature swing adsorption (TSA) can be used. Golmakani et al. [26] found that the PVSA method exhibits superior performance with respect to recovery, purity, productivity and energy consumption, compared to the other two cyclic methods for ultra-pure hydrogen production.

Reduction of the energy consumption and increase of hydrogen recovery and productivity of the PVSA process are required, and could potentially be addressed by development of

sorbents with relatively high removal efficiencies for CH_4 , CO , CO_2 , and N_2 ; however, developing such adsorbents is still challenging. This study investigates the effect of impurities on hydrogen recovery, productivity and energy consumption, in order to identify the most critical impurities, which would lead to development of adsorbents with higher adsorption capacity towards those impurities. Accordingly, a 4-bed PVSA process with 16 steps was designed, in which each adsorption bed consisted of two layers—activated carbon and zeolite 5A. The concentration profiles of various impurities along the activated carbon and zeolite layers were simulated to evaluate the removal efficiencies of the layers for the tested impurities, and to identify the most critical impurities, i.e., those with the highest concentrations at the outlet of the adsorption bed. Furthermore, since it is known that N_2 is the most critical impurity, purification of two feeds with different concentrations of N_2 were simulated to explore their effect on the PVSA process performance parameters (hydrogen purity, productivity, recovery, and energy consumption).

2. Process Description

A schematic of a SMR hydrogen production plant is presented in Figure 1. The product from the SMR unit enters the PVSA unit at a pressure higher than 22 bar and this PVSA unit produces hydrogen with 99.99 vol% purity for use in fuel cells. The composition of syngas from the SMR unit differs according to the technology provider, since each licensor of SMR units has different catalysts and different operating conditions. The typical nitrogen concentration in syngas is 1-3% [26,28] and, therefore, two feeds with nitrogen contents at the lower and upper limits were selected to investigate the effect of this impurity. The compositions of two feeds were 75% H_2 , 18% (20%) CO_2 , 3.2% CH_4 , 0.7% CO , and 3.1% (1.1%) N_2 (vol%).

Figure 2 illustrates different time steps for the proposed PVSA process. The first step of the PVSA process is adsorption and providing purge (AD & PPG). Two equalisation steps are applied to increase recovery of hydrogen. At the time when one of the beds is at the first depressurisation step (ED1), another bed is being pressurised for the second stage (EP2). At the second depressurisation step (ED2) of the aforementioned bed, the other bed is at its first pressurising stage (EP1). Blow down (BD) and vacuum (VA) steps are used for regenerating the beds. The purge step (PG) is implemented under vacuum conditions in order to regenerate the beds more efficiently.

Figure 3 illustrates the 4 main steps of a cycle. At the first step ($A1 = 10$ s), beds 1 and 2 are at adsorption (AD) and blow down (BD), respectively, while, beds 3 and 4 are at equalisation, i.e., bed 3 is in the second pressurisation (EP2) and bed 4 is in the first depressurisation (ED1). At the second step ($A2 = 20$ s), the conditions of all beds are the same, except for bed 2, which is under vacuum (VA). At the third step ($A3 = 40$ s), bed 1 is still in adsorption, and also providing purge (AD&PPG) for regeneration of bed 2, which is at purge (PG). At the same time, the conditions of beds 3 and 4 are the same as those during the previous step (EP2, ED1, respectively). At the fourth step ($A4 = 20$ s), beds 2 and 4 are connected to each other; bed 2 is in the first pressurisation (EP1) and bed 4 is in the second depressurisation (ED2), and bed 3 is being re-pressurised (RP) by the inlet feed stream. Following the same sequence of the same time steps, but with different beds, the cycle continues with step B1 and it is completed with step D4 [26].

The simulated small-scale PVSA unit consists of 4 beds and each bed has two layers, activated carbon and zeolite 5A, respectively, with the bed specifications presented in Table 1.

3. Process Simulation and Modelling

The assumptions used for modelling in this study are summarised below:

- 1- Peng-Robinson equation of state was used for gas phase.
- 2- Constant and uniform bed and particle porosity is considered for each layer.
- 3- Axially-dispersed plug-flow was considered.
- 4- Radial gradients of heat and mass were neglected.
- 5- Ergun equation was used for estimating pressure drop along bed.
- 6- Gas-to-particles mass transfer was measured by a solid linear driving force model.
- 7- Extended Langmuir was considered for adsorption isotherms.
- 8- The particle and gas phase temperatures are different.

The governing equations used for simulating the PVSA process are reported in Table 2. These partial differential equations (PDEs) were converted to ordinary differential equations (ODEs) and the implicit Euler method was used for solving them. The finite difference method was used for discretisation of spatial first and second derivatives. Each bed was divided into 50 nodes and the time interval for solving ODEs was 1 s. The Langmuir model parameters and linear driving force (LDF) coefficients for each gas are presented in Table A1 of the Appendix [39]. The boundary and initial conditions for each step are summarised in Table A2 of the Appendix. Cyclic steady state (CSS) conditions are obtained at a relative tolerance of 10^{-6} for product composition in 2 successive cycles. The process model was validated according to the experimental data presented in our previous study [26].

Hydrogen purity (vol%) and concentration of CO (ppm) in the product at the CSS conditions are calculated using Eq. (8) and Eq. (9):

$$\text{Purity (\%)} = \frac{\int_0^{t_{\text{ads}}} C_{\text{H}_2\text{P}} u_{\text{sp}} dt}{\sum_{i=1}^n \int_0^{t_{\text{ads}}} C_{\text{ip}} u_{\text{sp}} dt} \times 100$$

8

$$CO \text{ (ppm)} = \frac{\int_0^{t_{ads}} C_{COP} u_{sp} dt}{\sum_{i=1}^n \int_0^{t_{ads}} C_{ip} u_{sp} dt} \times 10^6 \quad 9$$

where C_{H_2P} and C_{COP} are hydrogen and carbon monoxide concentrations at the bed outlet, respectively, C_{ip} is component i concentration at outlet of bed and u_{sp} is superficial velocity at product end. The recovery is a good performance indicator for estimating the efficiency of a PVSA process because it represents the ratio of produced hydrogen with the fuel cell specification and hydrogen that enters the bed, and it is calculated by Eq. (10):

$$\text{Recovery} = \frac{\int_0^{t_{ads}} C_{H_2P} u_{sp} dt - \int_0^{t_{purge}} C_{H_2P} u_{spurge} dt}{\int_0^{t_{ads}} C_{H_2f} u_{sfeed} dt + \int_0^{t_{repress}} C_{H_2f} u_{sfeed} dt} \quad 10$$

where u_{sfeed} is feed end superficial velocity and u_{spurge} is superficial velocity at the inlet of bed during the purge step. Another criterion for measuring performance of a plant is productivity, Eq. (11). It indicates the hydrogen production in a cycle per unit of adsorbent weight.

$$\text{Productivity} = \frac{\left(\int_0^{t_{ads}} C_{H_2P} u_{sp} dt - \int_0^{t_{purge}} C_{H_2P} u_{spurge} dt \right) A_{bed}}{t_{cycle} W_{ads}} \quad 11$$

The power consumption in vacuum and purge steps is calculated by Eq. (12) [42]:

$$\text{Power}_{va}(W) = \frac{\gamma}{\gamma - 1} R_g T_{gf} \left[\left(\frac{P_{atm}}{P_{va}} \right)^{\frac{\gamma-1}{\gamma}} - 1 \right] u_{sfeed} C_{feed,T} \pi R_{Bi}^2 \quad 12$$

The average required energy is calculated by Eq. (13):

$$\text{Energy}_{avg} \left(\frac{j}{\text{mol } H_2 \text{ prod.}} \right) = \frac{\int_0^{t_{va}+t_{pg}} \text{Power}_{va} dt}{\left(\int_0^{t_{ads}} C_{H_2P} u_{sp} dt - \int_0^{t_{purge}} C_{H_2P} u_{spurge} dt \right) A_{bed}} \quad 13$$

4. Results and discussion

The simulation results of the PVSA process for two feeds which produce hydrogen with fuel cell specifications are provided in Table 3. All the runs were performed by the PVSA method with steps presented in Figures 2 and 3. The simulation results of the first feed with the

higher nitrogen concentration (3.1% N₂) is presented in run 1 and those for the second feed, with 1.1% N₂, are presented in runs 2 and 3.

Each run in Table 3 is performed for several cycles, and after reaching CSS conditions the purity, recovery, productivity, and energy consumption are calculated. Figure 4 shows the purity of produced hydrogen and recovery at successive cycles for Run 1. It can be seen that after each cycle the purity decreases until it reaches 99.99%, and the recovery increases reaching a maximum at the CSS conditions.

Runs 1 and 2 have the same conditions including the length of activated carbon and zeolite layers, purge-to-feed ratio, and vacuum level, and only differ in N₂ and CO₂ concentrations. As the hydrogen purity of run 2 satisfied the required specification for fuel cells (>99.99% H₂), in run 3, the purge-to-feed ratio was decreased to generate a larger recovery and productivity, and reduced energy consumption, but still to meet the fuel cell specification of hydrogen purity.

The performance parameter results of the second feed (runs 2 and 3) with 1.1 vol% N₂ are better than those for the first feed with 3.1 vol% N₂, especially with respect to recovery and energy consumption, and it can be concluded that nitrogen content in the feed is an important parameter for ultra-pure hydrogen production meeting required specifications of fuel cells.

In order to understand the effect of nitrogen concentration in the feed gas on the purity of produced hydrogen, the impurity concentrations along each adsorbent layer were investigated. The concentration profiles of impurities along the activated carbon layer are provided in Figure 5a. It can be seen that major portions of CO₂ and CH₄ are removed from the gas at the bed inlet, but N₂ and CO elute to the bed end. In Figure 5b, the concentrations

at the bed end have been plotted and it is observed that nitrogen is the main impurity, and its concentration is much higher compared to other impurities.

To obtain a product within fuel cell specifications, a larger reduction in the nitrogen concentration is required ($<0.01\% \text{ N}_2$). The low adsorption capacity of activated carbon for N_2 is a barrier for ultra-pure hydrogen and, therefore, a second layer with relatively higher adsorption capacity toward N_2 is necessary. Zeolite 5A is a commercial adsorbent currently used in industrial units for this purpose. In Figure 6a, the concentration of all impurities along the zeolite layer at the end of the adsorption step are depicted, and it is observed that nitrogen concentration is still much higher than that of other impurities. It can be seen that the fraction of all other impurities is negligible, confirming that the activated carbon layer, as the first layer, properly removed them. Their concentrations along the zeolite layer at the end of the adsorption step are depicted in Figure 6b, which shows that half of the zeolite layer is enough to remove all the remaining CO_2 , and full length of the zeolite layer was needed to lower the CO concentration to 0.2 ppm. These results further highlight the importance of having an adsorbent with a higher affinity towards nitrogen. Namely, despite its relatively low concentration ($3.1\% \text{ N}_2$) compared to total concentration of other impurities ($21.9\% \text{ CO}_2 + \text{CH}_4 + \text{CO}$), nitrogen is almost the sole impurity at bed outlet.

In order to explore the evolution of adsorption of impurities along the zeolite layer, their mole fractions along this layer from the start to the end of the adsorption step are depicted in Figure 7. It can be observed that the concentration of all impurities along the zeolite layer increases during the adsorption step, indicating that the activated carbon layer is being saturated, but the rates of increase for N_2 and CO (Figures 7b and 7c) are much higher than those for CO_2 and CH_4 (Figures 7a and 7d).

Figures 7a and 7d show that the concentrations of CO_2 and CH_4 approach zero at the end of the adsorption step at the mid-point of the zeolite layer. It is expected that impurity

concentrations decrease along the zeolite layer, which occurs for all impurities except nitrogen, for which the concentration decreases up to the middle of bed and then increases. To understand the reason for this phenomenon, the loading of nitrogen at the pressurisation steps (EP1, EP2 and RP), adsorption (AD) and purge (PG) steps is depicted in Figure 8b. It is observed that during the re-pressurisation step (RP), the loading of adsorbent at approximately the second half of the bed is higher than that at the adsorption step (AD), which implies that the adsorbent at the second half of the bed starts to desorb the nitrogen during the adsorption step, and this causes the nitrogen concentration to increase at the bed end.

In Figure 8a, the nitrogen loading at various steps has been depicted. It is observed that during the depressurisation steps and even vacuum step, the loading of nitrogen increases along the zeolite layer, which shows that the bed is more saturated by nitrogen instead of being regenerated. In order to understand this behaviour, it is necessary to study the loading of the first layer. Figure 9 presents the loadings of different impurities in the activated carbon layer, which decrease during depressurisation steps. To understand why nitrogen concentration increased during the depressurisation steps along the zeolite layer (Figure 8), it should be considered that all the nitrogen, which was adsorbed by the activated carbon layer, is being desorbed during depressurisation. This nitrogen is adsorbed by the zeolite layer, which causes the nitrogen loading along this layer to increase. By comparing Figures 8 and 9, it can be concluded that the purge step is necessary for the zeolite layer, because at this step, this layer is being regenerated, while for activated carbon, the vacuum step also regenerates the bed, and the purge step does not contribute as much to bed regeneration.

Figure 9a depicts the loading of CO_2 along the activated carbon layer. It is observed that the CO_2 loading is maximum at the inlet of the bed, but continuously decreases along the bed layer, and at the end of the bed approaches almost zero, which indicates the majority of the CO_2 is removed at the beginning of the bed. It is also observed during depressurisation stages that the CO_2 loading does not change as much in comparison to the adsorption step, which shows that lower pressure is needed for CO_2 to start to desorb. At the blow down step, the CO_2 loading at the bed inlet decreases about 35% compared to the adsorption step and, after vacuum and purge steps, CO_2 loading decreases about 65% and 85%, respectively, which confirms these steps are regenerating the bed efficiently and the adsorbents at the bed inlet, which adsorb mostly CO_2 , are regenerated to a reasonable extent.

Figure 9b shows the CH_4 loading along the bed at various steps. Approximately half the bed is required to remove the CH_4 from the feed. In addition, negligible loading values at the end of the bed indicate there is not much CH_4 left in the gas stream. Moreover, since adsorbents have higher affinity for CO_2 , the maximum loading of CH_4 occurs at some distance from the inlet, where CO_2 concentration has already decreased. It is observed that during depressurisation steps (ED1, ED2), the CH_4 loading decreases since the bonding of CH_4 molecules to the adsorbents is weaker than for CO_2 . It is also observed that the CH_4 loading at the bed inlet decreases, while it increases at the bed outlet during depressurisation steps (ED1, ED2). In other words, the adsorbent at the end of the bed is adsorbing CH_4 during depressurisation steps while desorbing CH_4 at the bed inlet. The blow down and vacuum steps regenerated the bed sufficiently as the loading decreased considerably in each of these stages. However, the purge step did not have a noticeable effect on the bed regeneration.

Figure 9c shows the CO loading along the activated carbon bed. Unlike CH₄ and CO₂ with extremely low loading values over the second half of the bed, almost the entire bed length is used for removing CO during the adsorption step. During depressurisation steps, the CO loading at the bed inlet decreases, showing that it is regenerated. However, it can be seen that at the end of the bed, the CO loading is higher when compared to the adsorption step, indicating that during depressurisation steps (ED1, ED2), the adsorbents at the outlet of the bed are adsorbing CO. The use of the blow down step also cannot decrease the CO loading at the bed end; the CO loading is still higher than that of the adsorption step. However, the vacuum and purge steps cause the CO loading at the bed end to decrease, i.e. adsorbent is being regenerated. It is observed that at the end of the re-pressurisation step (RP), the loading of CO at the bed inlet (length < 0.1 m) is higher compared to the end of the adsorption step, which means that during AD, CO is being desorbed at the bed inlet, while being adsorbed at bed end. The reason for this phenomenon is that the adsorbent at the bed inlet has a greater tendency to adsorb CO₂ and CH₄; therefore, at the beginning of the adsorption step, CO is being desorbed at the inlet of the bed. Consequently, all the bed is used for removing CO, which is adsorbed mainly near the end of the bed.

The N₂ loading of activated carbon along the bed is given in Figure 9d. It is observed that N₂ and CO have the same pattern during depressurisation steps, i.e., N₂ is desorbed at the beginning of the bed and is adsorbed at the bed end. The vacuum and purge steps are mandatory for regeneration of adsorbent at the bed end.

The loading of various gases along the activated carbon bed at the end of the adsorption step is provided in Figure 10a. It can be seen that at the inlet of the bed, CO₂ has the highest loading and CO has the lowest loading value, while at the bed end the maximum and

minimum loading values are for N_2 and CH_4 , respectively. The reason for low loading of CH_4 at the end of the bed is attributed to its relatively low concentration in the gas phase. In addition, the majority of CH_4 is removed at the inlet of the bed. On the other hand, the high loading of N_2 at the end of the bed indicates that it has not been adsorbed along the activated carbon layer.

According to the results presented in this study, it can be concluded that that nitrogen removal is more challenging than other impurities of syngas. In order to explore further the nitrogen effect on ultra-pure hydrogen production, purification of two syngas feeds was simulated and the results on purity, recovery, productivity and energy consumption were compared in Table 3. It was calculated that the first feed (run 1) produces hydrogen with 99.990% purity and CO concentration of 0.19 ppm; the recovery is about 47%, and the energy consumption is 940 kJ/kg_{H₂Prod.}. The performance parameters for the second feed (run 2) show that purity of produced hydrogen (99.997%) is much higher than hydrogen produced from the first feed. For fuel cell application, the required purity for hydrogen is 99.99%; therefore, in run 3, the purge-to-feed ratio was decreased to 10% (from 25%) and it is observed that hydrogen of 99.991% purity is produced. The re-calculated result of the second feed (Run 3) shows 55% H₂ recovery while the recovery from the first feed (Run 1) is 47%. The energy consumption for the second feed (Run 3) is 430 kJ/kg_{H₂Prod.}, which is about half that for the first feed (run 1).

Figure 11 shows the fraction of nitrogen impurity along the zeolite layer for two different feeds (run 1 and 2). The fraction of nitrogen at the bed outlet for run 2 is less than one third

of the value for run 1, which results in a higher hydrogen purity for run 2 (99.997 vol%) compared to run 1 (99.990 vol%).

5. Conclusions

The PVSA process is currently the most established method to produce fuel-cell-purity hydrogen, but it is energy intensive, and interest in reducing the energy consumption by this process is growing. In this study, a 4-bed PVSA process model, with 16 steps including two equalisation steps for increasing recovery, was developed. Each bed consisted of two layers (activated carbon (AC)/zeolite 5A), a portion of the product was used for bed purging during the regeneration step, and the re-pressurisation step for each bed was implemented with the feed. The concentration profiles of all considered impurities were simulated, and it was found that the AC layer was sufficient for removing CH_4 , CO_2 , and CO . Zeolite as a second layer was required mostly to remove the remaining N_2 , which was not sufficiently efficient and N_2 was the sole impurity at the bed outlet. The effect of N_2 impurity on PVSA performance was further investigated by simulating two feeds with 3.1% and 1.1% N_2 . It was found that the energy consumption of the PVSA process for feed with 1.1% N_2 was 430.5 $\text{kJ/kg}_{\text{H}_2\text{Prod.}}$, about 55% lower than that required for feed with 3.1% N_2 (940.1 $\text{kJ/kg}_{\text{H}_2\text{Prod.}}$). Also, the H_2 recovery from feed with 1.1% N_2 was 55%, which is 8% higher than that from feed with 3.1% N_2 (47%). Considering these results, the nitrogen in syngas entering the PVSA process is the most critical impurity; therefore, natural gas/syngas sources containing less nitrogen are required for producing hydrogen at lower costs. Finally, production of new adsorbents with higher affinity toward nitrogen can significantly reduce the energy consumption required for ultra-pure hydrogen production.

References

- [1] E.H. Majlan, W.R. Wan Daud, S.E. Iyuke, A.B. Mohamad, A.A.H. Kadhum, A.W. Mohammad, M.S. Takriff, N. Bahaman, *Int. J. Hydrogen Energy* 34 (2009) 2771–77.
<https://doi.org/10.1016/j.ijhydene.2008.12.093>.
- [2] B.M. Besancon, V. Hasanov, R. Imbault-Lastapis, R. Benesch, M. Barrio, M.J. MølInvik, *Int. J. Hydrogen Energy* 34 (2009) 2350–60. <https://doi.org/10.1016/j.ijhydene.2008.12.071>.
- [3] S.K. Park, T.S. Kim, J.L. Sohn, Y.D. Lee, *Appl. Energy* 88 (2011) 1187–96.
<https://doi.org/10.1016/j.apenergy.2010.10.037>.
- [4] J.D. Scheelhaase, *J. Air Transp. Manag.* 75 (2019) 68–74.
<https://doi.org/10.1016/j.jairtraman.2018.11.007>.
- [5] S.-Y. Lee, S.-J. Park, *J. Ind. Eng. Chem.* 23 (2015) 1–11.
<https://doi.org/10.1016/j.jiec.2014.09.001>.
- [6] G. Zhang, J. Qu, Y. Du, F. Guo, H. Zhao, Y. Zhang, Y. Xu, *J. Ind. Eng. Chem.* 20 (2014) 2948–57.
<https://doi.org/10.1016/j.jiec.2013.10.064>.
- [7] S. Sircar, T.C. Golden, *Sep. Sci. Technol.* 35 (2000) 667–87. <https://doi.org/10.1081/SS-100100183>.
- [8] F.V.S. Lopes, C.A. Grande, A.E. Rodrigues, *Fuel* 93 (2012) 510–23.
<https://doi.org/10.1016/j.fuel.2011.07.005>.
- [9] Y.-N. Wang, A.E. Rodrigues, *Fuel* 84 (2005) 1778–89.
<https://doi.org/10.1016/j.fuel.2005.04.005>.
- [10] J. Gao, M. Li, Y. Hu, H. Chen, Y. Ma, *Sci. China Inf. Sci.* 62 (2019) 51201.
<https://doi.org/10.1007/s11432-018-9690-y>.
- [11] A.M. Ribeiro, C.A. Grande, F.V.S. Lopes, J.M. Loureiro, A.E. Rodrigues, *Chem. Eng. Sci.* 63 (2008) 5258–73. <https://doi.org/10.1016/j.ces.2008.07.017>.
- [12] A. Saeedmanesh, P. Colombo, D. McLarty, J. Brouwer, *J. Electrochem. Energy Convers. Storage* 16 (2019). <https://doi.org/10.1115/1.4043340>.

- [13] Q. Lei, B. Wang, P. Wang, S. Liu, J. Energy Chem. (2019) 162–69.
<https://doi.org/10.1016/j.jechem.2018.12.022>.
- [14] M. Tayebi, B.-K. Lee, Renew. Sustain. Energy Rev. 111 (2019) 332–43.
<https://doi.org/10.1016/j.rser.2019.05.030>.
- [15] M. Liao, Y. Chen, Z. Cheng, C. Wang, X. Luo, E. Bu, Z. Jiang, B. Liang, R. Shu, Q. Song, Appl. Energy 252 (2019). <https://doi.org/10.1016/j.apenergy.2019.113435>.
- [16] M. Steinberg, Energy Convers. Manag. 36 (1995) 791–96. [https://doi.org/10.1016/0196-8904\(95\)00123-U](https://doi.org/10.1016/0196-8904(95)00123-U).
- [17] A.A. Shamsabadi, A. Kargari, M.B. Babaheidari, S. Laki, J. Ind. Eng. Chem. 19 (2013) 1680–88.
<https://doi.org/10.1016/j.jiec.2013.02.006>.
- [18] S. Saeidi, F. Fazlollahi, S. Najari, D. Iranshahi, J.J. Klemeš, L.L. Baxter, J. Ind. Eng. Chem. 49 (2017) 1–25. <https://doi.org/10.1016/j.jiec.2016.12.003>.
- [19] G. Diglio, D.P. Hanak, P. Bareschino, F. Pepe, F. Montagnaro, V. Manovic, Appl. Energy 210 (2018) 1–15. <https://doi.org/10.1016/j.apenergy.2017.10.101>.
- [20] D.D. Nguyen, S.I. Ngo, Y.-I. Lim, W. Kim, U.-D. Lee, D. Seo, W.-L. Yoon, Int. J. Hydrogen Energy 44 (2019) 1973–87. <https://doi.org/10.1016/j.ijhydene.2018.11.188>.
- [21] S. Cavenati, C.A. Grande, A.E. Rodrigues, J. Chem. Eng. Data 49 (2004) 1095–101.
<https://doi.org/10.1021/je0498917>.
- [22] Z. Zhang, W. Zhang, X. Chen, Q. Xia, Z. Li, Sep. Sci. Technol. 45 (2010) 710–19.
<https://doi.org/10.1080/01496390903571192>.
- [23] T.L.P. Dantas, F.M.T. Luna, I.J. Silva Jr, D.C.S. de Azevedo, C.A. Grande, A.E. Rodrigues, R.F.P.M. Moreira, Chem. Eng. J. 169 (2011) 11–19. <https://doi.org/10.1016/j.cej.2010.08.026>.
- [24] P. Brea, J.A. Delgado, V.I. Águeda, M.A. Uguina, Chem. Eng. J. 355 (2019) 279–89.
<https://doi.org/10.1016/j.cej.2018.08.154>.
- [25] A. Abdeljaoued, F. Relvas, A. Mendes, M.H. Chahbani, J. Environ. Chem. Eng. 6 (2018) 338–55.
<https://doi.org/10.1016/j.jece.2017.12.010>.

- [26] A. Golmakani, S. Fatemi, J. Tamnanloo, *Sep. Purif. Technol.* 176 (2017) 73–91.
<https://doi.org/10.1016/j.seppur.2016.11.030>.
- [27] J. Zhong, X. Meng, *Pet. Refin. Eng.* 49 (2019) 35–37 and 42.
<https://www.scopus.com/inward/record.uri?eid=2-s2.0-85065061722&partnerID=40&md5=438315adb1c13957ecf358e9ee>.
- [28] W. Tao, S. Ma, J. Xiao, P. Bénard, R. Chahine, *Energy Procedia*, 158 (2019) 1917–23.
<https://doi.org/10.1016/j.egypro.2019.01.441>.
- [29] J. Xiao, L. Fang, P. Bénard, R. Chahine, *Int. J. Hydrogen Energy* 43 (2018) 13962–74.
<https://doi.org/10.1016/j.ijhydene.2018.05.054>.
- [30] W. Shi, H. Yang, Y. Shen, Q. Fu, D. Zhang, B. Fu, *Int. J. Hydrogen Energy* 43 (2018) 19057–74.
<https://doi.org/10.1016/j.ijhydene.2018.08.077>.
- [31] Q. Huang,, M. Eić, in: M. Fan, C.-P. Huang, A. E. Bland, Z. Wang, R. Slimane, I. B. T.-E. Wright (Eds.), Elsevier, Amsterdam, 2010, pp. 221–44.
- [32] F.V.S. Lopes, C.A. Grande, A.E. Rodrigues, *Chem. Eng. Sci.* 66 (2011) 303–17.
<https://doi.org/10.1016/j.ces.2010.10.034>.
- [33] International Energy Agency, Hydrogen and fuel cells. Review of national R and D programs.
<https://www.forskningsdatabasen.dk/en/catalog/2389484980>, 2004.
- [34] F.C.S. Committee, Information Report on the Development of a Hydrogen Quality Guideline for Fuel Cell Vehicles, SAE, J2719, *Int. Organ. Stand. Hydrog. Fuel–Product Specif.* 2 (n.d.) 14682–14687. https://www.sae.org/standards/content/j2719_200804/
- [35] S. IOF, Hydrogen fuel–product specification–Part 2: proton exchange membrane (PEM) fuel cell applications for road vehicles, ISO/TS, 2012, pp.14682–14687.
- [36] S.E. Iyuke, W.R.W. Daud, A.B. Mohamad, A.A.H. Kadhun, Z. Fisal, A.M. Shariff, *Chem. Eng. Sci.* 55 (2000) 4745–55. [https://doi.org/10.1016/S0009-2509\(99\)00602-8](https://doi.org/10.1016/S0009-2509(99)00602-8).
- [37] C. Lu, H. Bai, B. Wu, F. Su, J.F. Hwang, *Energy & Fuels* 22 (2008) 3050–56.
<https://doi.org/10.1021/ef8000086>.
- [38] J. Tamnanloo, S. Fatemi, A. Golmakani, *Adsorpt. Sci. Technol.* 32 (2014) 707–16.

<https://doi.org/10.1260/0263-6174.32.9.707>.

- [39] S. Ahn, Y.-W. You, D.-G. Lee, K.-H. Kim, M. Oh, C.-H. Lee, Chem. Eng. Sci. 68 (2012) 413–23.

<https://doi.org/10.1016/j.ces.2011.09.053>

- [40] J. Yang, C. Lee, AIChE J. 44 (1998) 1325–34. <https://doi.org/10.1002/aic.690440610>.

- [41] C. Sereno, A. Rodrigues, Gas Sep. Purif. 7 (1993) 167–74. [https://doi.org/10.1016/0950-](https://doi.org/10.1016/0950-4214(93)80006-I)

4214(93)80006-I.

- [42] Z. Liu, C.A. Grande, P. Li, J. Yu, A.E. Rodrigues, Sep. Purif. Technol. 81 (2011) 307–17.

<https://doi.org/10.1016/j.seppur.2011.07.037>.

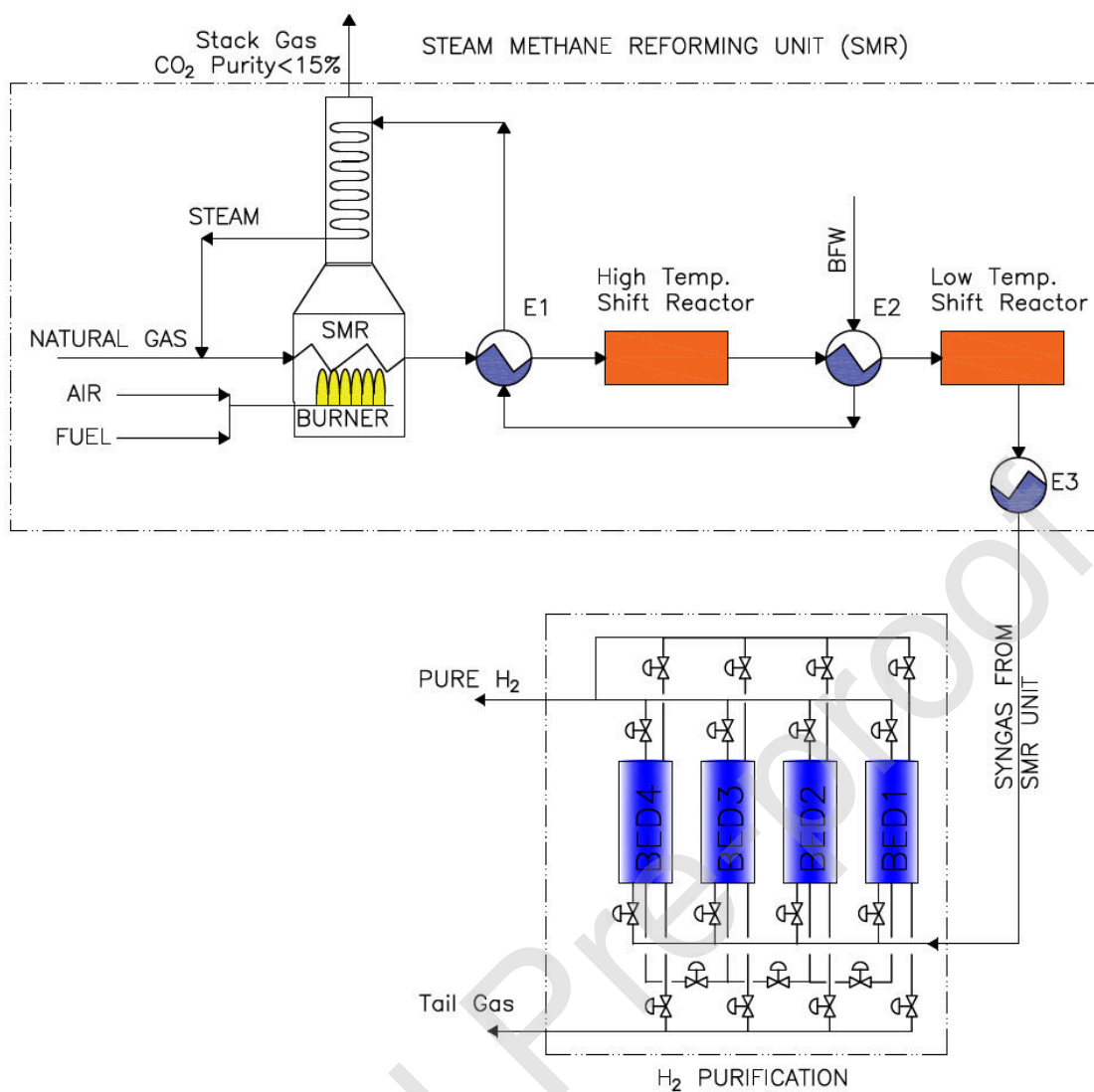
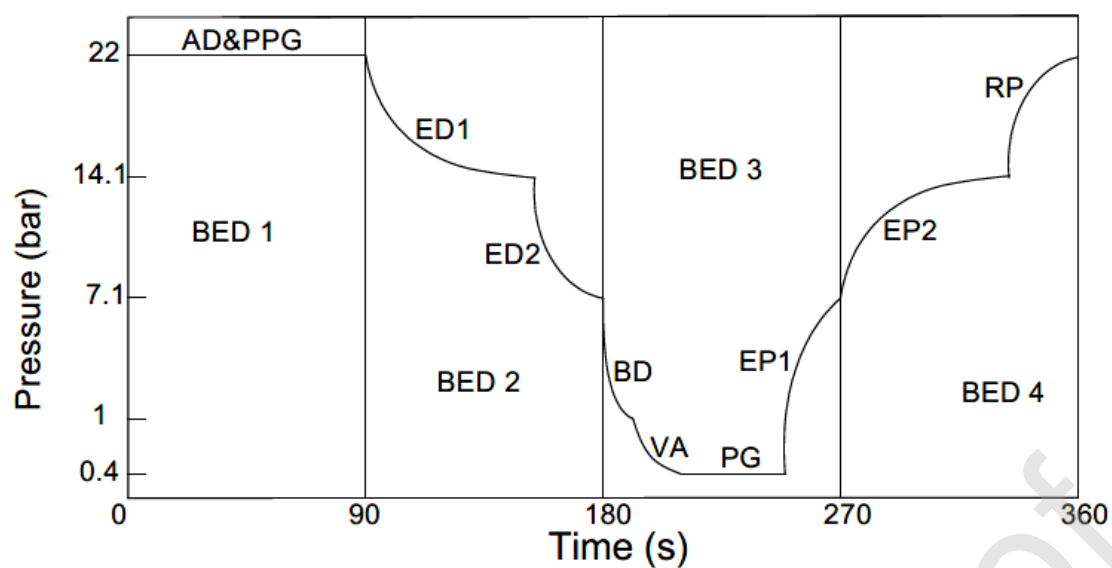


Figure 1. Schematic of SMR plant/PVSA unit. BFW: Boiler feed water, E: Exchanger.



PVSA STEPS				
BED1	AD&PPG	ED1/ED2	BD/VA/PG/EP1	EP2/RP
BED2	BD/VA/PG/EP1	EP2/RP	AD&PPG	ED1/ED2
BED3	EP2/RP	AD&PPG	ED1/ED2	BD/VA/PG/EP1
BED4	ED1/ED2	BD/VA/PG/EP1	EP2/RP	AD&PPG
$t = t = 70 \text{ s}$ $t = t = t = t = 20 \text{ s}$ $t = 10 \text{ s}$ $t = 90 \text{ s}$ $t = 40 \text{ s}$ ED1 EP2 ED2 EP1 RP VA BD AD&PPG PG				

Figure 2. PVSA pressure profile and time table, AD: adsorption, AD&PPG: adsorption and providing purge, BD: blow down, ED1: first equalisation depressurisation, ED2: second equalisation depressurisation, EP1: first equalisation pressurisation, EP2: second equalisation pressurisation, RP: repressurisation, PG: purge, VA: vacuum.

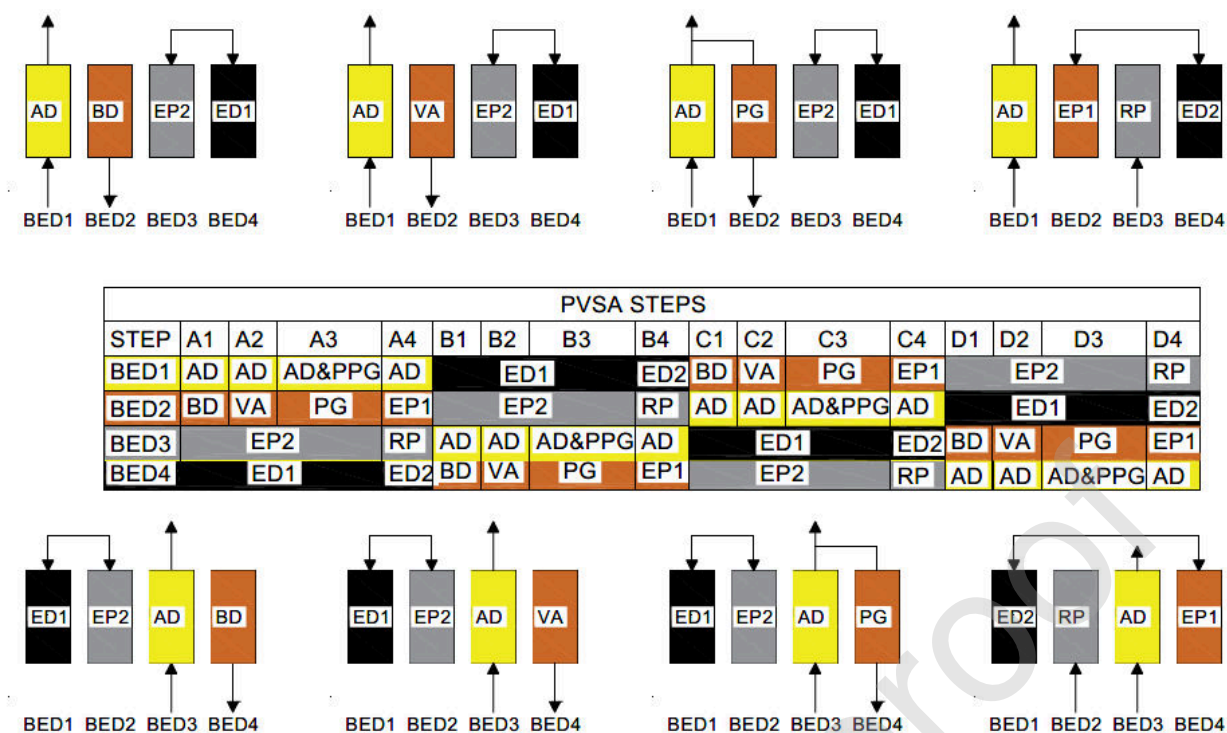


Figure 3. Schematic presentation of PVSA process steps for two time-steps, A and B. Abbreviations are the same as those in Figure 2.

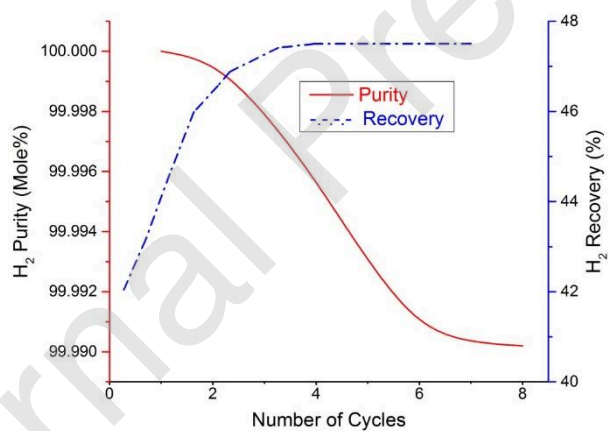


Figure 4. The purity and recovery at several successive cycles to CSS conditions for Run 1.

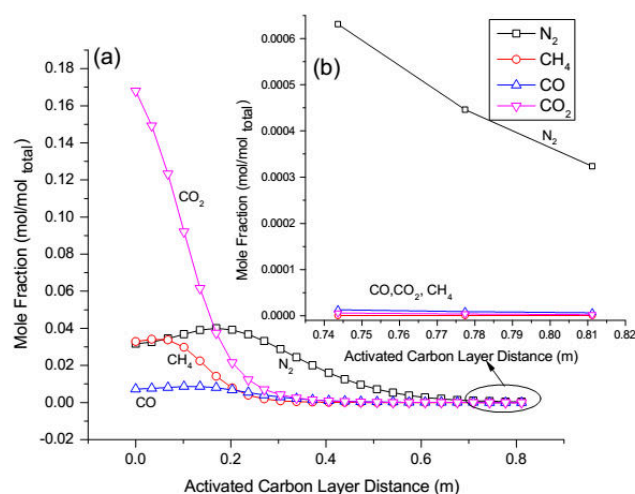


Figure 5. Mole fraction of impurities at end of adsorption step at CSS conditions for Run 1: (a) along activated carbon layer, and (b) at end of activated carbon layer.

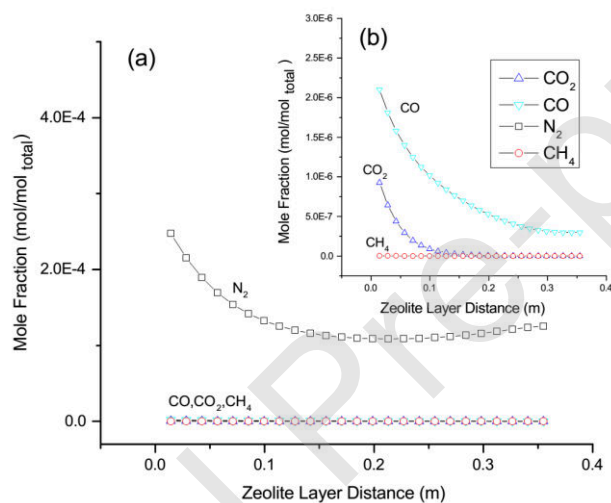


Figure 6. Mole fraction of impurities at end of adsorption step at CSS conditions for Run 1 along zeolite layer: (a) all impurities, (b) all except N_2 .

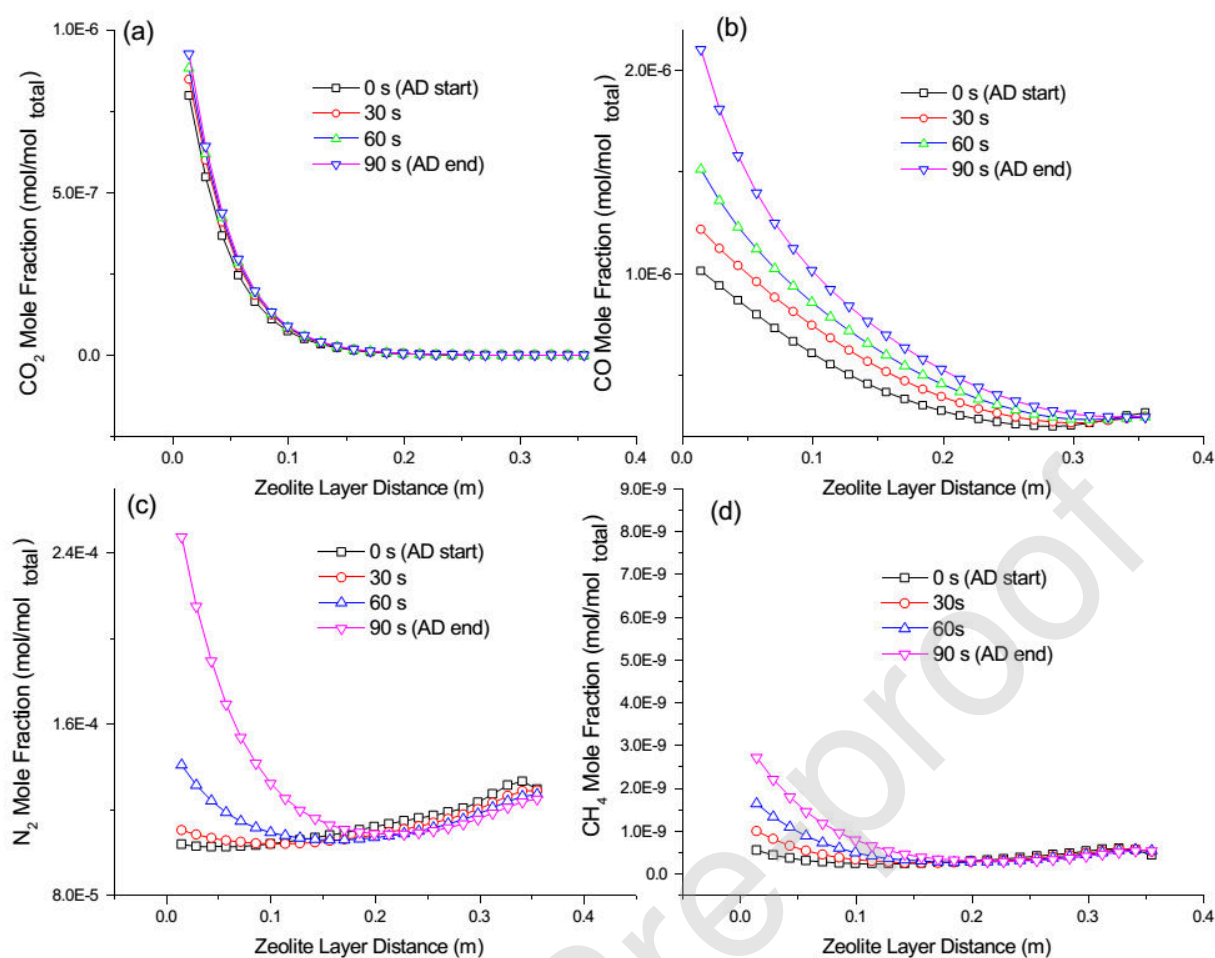


Figure 7. Mole fraction of impurities along zeolite layer at 30 s intervals during adsorption step at CSS conditions for Run 1: (a) CO_2 , (b) CO, (c) N_2 , and (d) CH_4 .

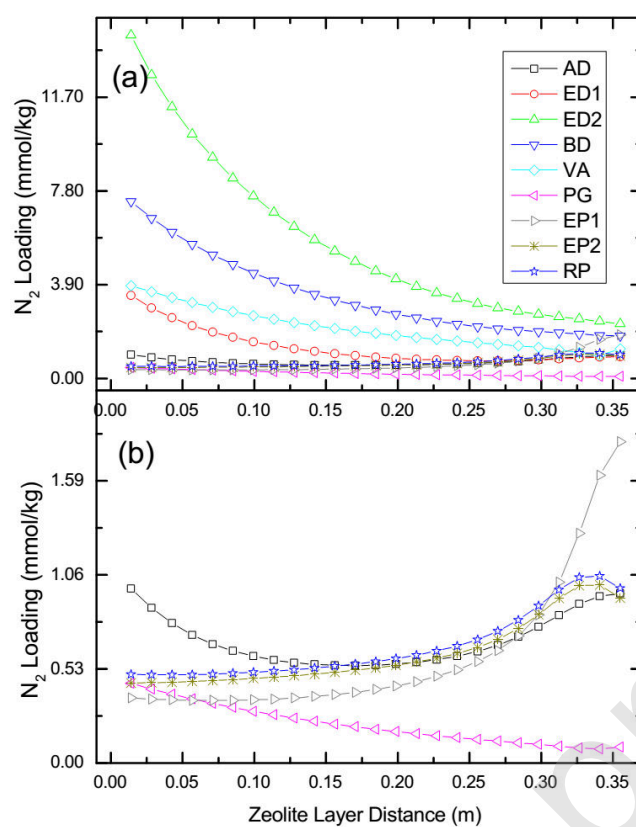


Figure 8. The nitrogen loading along the zeolite layer after CSS conditions (Run 1): (a) at various steps. (b) at AD, PG, EP1, EP2, RP steps. Abbreviations are the same as those in Figure 2.

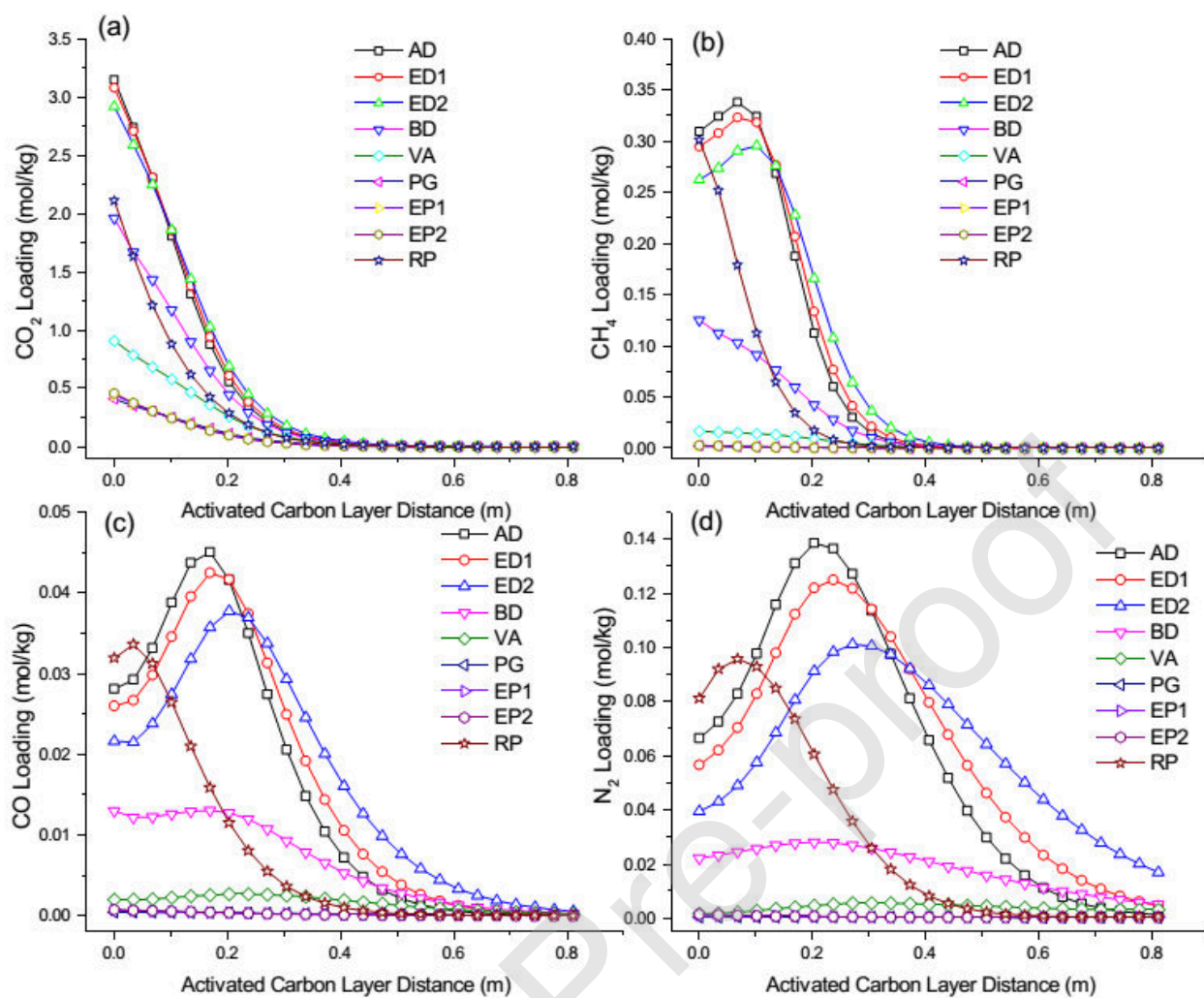


Figure 9. Impurities loading along activated carbon layer at various steps after CSS conditions for Run 1: (a) CO_2 , (b) CH_4 , (c) CO , and (d) N_2 .

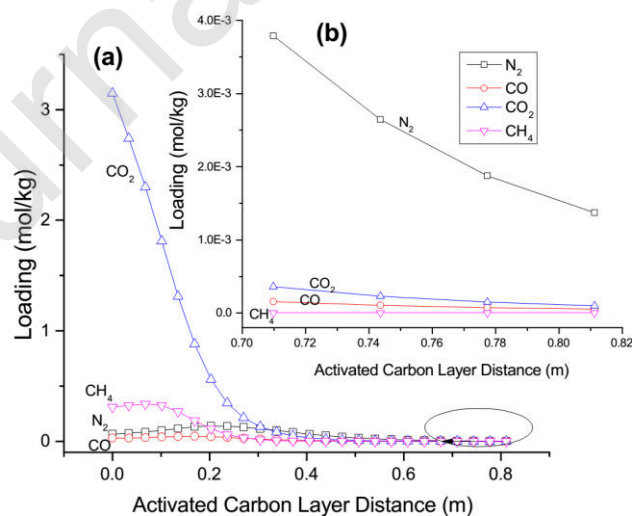


Figure 10. Impurities loading at end of adsorption step after CSS conditions for Run 1: (a) along activated carbon layer, and (b) at end of activated carbon layer.

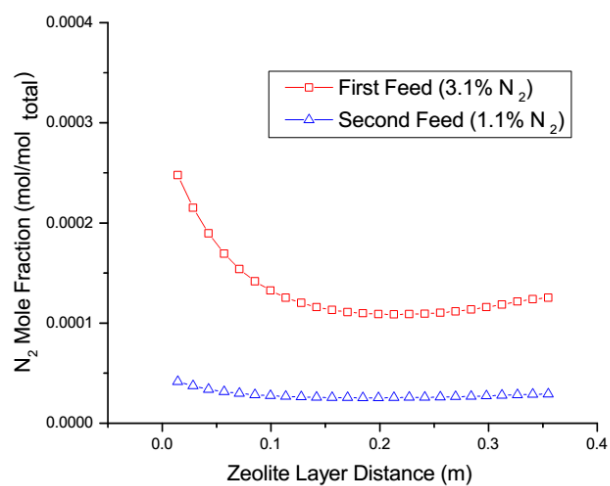


Figure 11. Mole fraction of nitrogen along zeolite layer after CSS conditions at end of adsorption step for two different feeds: first feed with 3.1% N_2 (Run 1), second feed with 1.1% N_2 Run (2).

Table 1. Specifications of bed and adsorbents.

Parameter	Value
Diameter of bed, D_B (cm)	3.5
Specific heat of wall, C_{pw} ($\frac{J}{kg\ K}$)	502.4
Density of wall, ρ_w ($\frac{kg}{m^3}$)	783
Density of particle, ρ_p ($\frac{kg}{m^3}$)	Activated carbon: 850, Zeolite 5A: 1160
Specific heat of particle, C_{ps} ($\frac{J}{kg\ K}$)	Activated carbon: 1047, Zeolite 5A: 920
Porosity of particle, ϵ_p (-)	Activated carbon: 0.61, Zeolite 5A: 0.65
Porosity of bed, ϵ (-)	Activated carbon: 0.433, Zeolite 5A: 0.357
Particle diameter, d_p (mm)	Activated carbon: 2.3, Zeolite 5A: 3.14
Bed length (cm)	Activated carbon: 84.5 cm, Zeolite 5A: 35.5 cm
Temperature of inlet feed (K)	303
Pressure of inlet feed (bar)	22
Volume fraction of feed (vol%)	First feed: 75% H ₂ , 18% CO ₂ , 3.2% CH ₄ , 0.7% CO, 3.1% N ₂ , Second feed: 75% H ₂ , 20% CO ₂ , 3.2% CH ₄ , 0.7% CO, 1.1% N ₂
Flow rate of feed (SLPM)	10

Table 2. Governing equations for PVSA simulations.

Description	Formulation	
component i mass balance in gas phase	$\frac{\partial}{\partial z} \left(\varepsilon D_{z,i} C_{gT} \frac{\partial y_i}{\partial z} \right) - \frac{\partial}{\partial z} (u_s C_{g,i}) - \varepsilon \frac{\partial C_{g,i}}{\partial t} - (1 - \varepsilon) \rho_p \frac{\partial q_i}{\partial t} = 0$	1
linear driving force (LDF) model	$\frac{\partial q_i}{\partial t} = \omega_i (q_i^* - q_i)$	2
gas mixture adsorption equilibrium	$q_i^* = \frac{(k_{1,i} + k_{2,i} T) k_{3,i} \exp\left(\frac{k_{4,i}}{T}\right) P_i}{1 + \sum_{i=1}^n k_{3,i} \exp\left(\frac{k_{4,i}}{T}\right) P_i}$	3
energy balance in gas phase	$\frac{\partial}{\partial z} \left(\lambda \frac{\partial T_g}{\partial z} \right) - C_{gT} C_p \frac{\partial (u_s T_g)}{\partial z} - \varepsilon C_{vT} \frac{\partial C_{gT}}{\partial t} - (1 - \varepsilon) a_p h_f (T_g - T_p) - \frac{4h_w}{D_B} (T_g - T_w) - \varepsilon C_{gT} C_v \frac{\partial T_g}{\partial t} = 0$	4
energy balance in solid phase	$(1 - \varepsilon) \left[\rho_p \sum_{i=1}^n q_i C_{v,ads,i} + \rho_p C_{ps} \right] \frac{\partial T_p}{\partial t} = \rho_b \sum_{i=1}^n (-\Delta H_{ads})_i \frac{\partial q_i}{\partial t}$	5
wall energy balance	$\rho_w C_{pw} A_w \frac{\partial T_w}{\partial t} = 2\pi R_{Bi} h_w (T_g - T_w) - 2\pi R_{Bo} h_o (T_w - T_\infty)$	6
pressure drop across bed (Ergun equation) [40,41]	$-\frac{\partial P}{\partial z} = \frac{150 \mu (1 - \varepsilon)^2}{d_p^2 \varepsilon^3} u_s + \frac{1.75 (1 - \varepsilon) \rho}{d_p \varepsilon^3} u_s u_s $	7

Table 3. Results of simulation of the PVSA process.

	Length (cm)			Purge to feed	Vacuum	H ₂ Purity	H ₂ Recovery	H ₂ Productivity	CO	Energy
Run	Total	Zeolite	Activated Carbon	%	bar	(vol%)	(%)	$\frac{mol\ H_2}{kg_{ads}day}$	(ppm)	$\frac{kJ}{kg_{H_2prod}}$
First feed (75% H ₂ , 18% CO ₂ , 3.2% CH ₄ , 0.7% CO, 3.1% N ₂)										
1	120	35.5	84.5	25	0.2	99.990	47.5	148.0	0.19	940.1
Second feed (75% H ₂ , 20% CO ₂ , 3.2% CH ₄ , 0.7% CO, 1.1% N ₂)										
2	120	35.5	84.5	25	0.2	99.997	46.8	148.0	0.14	850.1
3	120	35.5	84.5	10	0.2	99.991	55.1	159.1	0.16	430.5

Appendix:

Table A1: extended Langmuir isotherm parameters for Activated Carbon and Zeolite 5A [39]

	LDF coeff. ω_i	K_1 (mol/kg)	K_2 (mol kg ⁻¹ K ⁻¹)	K_3 (1/bar)	K_4 (K)
Activated Carbon					
CH ₄	0.19	23.86	-0.0562	0.00348	1159
N ₂	0.26	1.64	-0.00073	0.0545	326
CO	0.15	33.85	-0.0907	0.000231	1751
H ₂	0.7	16.94	-0.021	0.0000625	1229
CO ₂	0.035	28.79	-0.07	0.01	1030
Zeolite 5A					
CH ₄	0.147	5.833	-0.01192	0.000605	1731
N ₂	0.099	4.8133	-0.00668	0.000570	1531
CO	0.063	11.8454	-0.0313	0.0202	763
H ₂	0.7	4.314	-0.0106	0.002515	458
CO ₂	0.0135	10.03	-0.01858	1.5781	207

Table A2: The Boundary and initial conditions of each step for PVSA process

Initial conditions					
t=0 for $i \neq H_2$	$y_i = C_{g,i} = q_i = 0$	$y_{H_2} = 1$	$T_g = T_p = T_w = T_{inlet}$		
Blowdown Step					
outlet Y=0			Y=L		
	$\frac{\partial y_i}{\partial z} = 0$			$\frac{\partial y_i}{\partial z} = 0$	
$P(t) = P_{atm} + (P_{sbd} - P_{atm})e^{(-k_p t)}$				$u_s = 0$	
	$\frac{\partial T_g}{\partial z} = 0$			$\frac{\partial T_g}{\partial z} = 0$	
Adsorption step					
Bed inlet (Y=0)			Bed end (Y=L)		
$u_{sfeed} C_{feed,i} = u_s C_{g,i} - \varepsilon D_z C_{gT} \frac{\partial y_i}{\partial z}$			$\frac{\partial y_i}{\partial z} = 0$		
$P = P_{feed}$			$P = P_{exit}$		
$u_{sfeed} C_{feed,T} C_p T_{feed} = u_s C_{gT} C_p T_g - \lambda \frac{\partial T_g}{\partial z}$			$\frac{\partial T_g}{\partial z} = 0$		
Both equalisation depressurising steps (ED1 and ED2)					
Y=0			Y=L		
$\frac{\partial y_i}{\partial z} = 0$			$\frac{\partial y_i}{\partial z} = 0$		
$u_s = 0$			$P = P_H + (P_{equib.} - P_H)(1 - e^{-k_p t})$		
$\frac{\partial T_g}{\partial z} = 0$			$\frac{\partial T_g}{\partial z} = 0$		
purge step					
outlet Y=0			inlet Y=L		
$\frac{\partial y_i}{\partial z} = 0$			$u_{spurge} C_{purge,i} = u_s C_{g,i} - \varepsilon D_z C_{gT} \frac{\partial y_i}{\partial z}$		
			$P = P_{purge}$		

$\frac{\partial T_g}{\partial z} = 0$		$u_{spurge}C_{purge,i}C_P T_{feed} = u_s C_{gT} C_P T_g - \lambda \frac{\partial T_g}{\partial z}$
Both equalisation pressurising steps (EP1, EP2)		
Y=0	Y=L	
$\frac{\partial y_i}{\partial z} = 0$	$u_{seD}C_{eD,i} = u_s C_{g,i} - \varepsilon D_z C_{gT} \frac{\partial y_i}{\partial z}$	
$u_s = 0$	$P = P_H + (P_{equib.} - P_H)(1 - e^{-k_p t})$	
$\frac{\partial T_g}{\partial z} = 0$	$u_{seD}C_{eDT}C_P T_{eDT} = u_o C_{gT} C_P T_g - \lambda \frac{\partial T_g}{\partial z}$	
Re-pressurisation step with feed		
Bed inlet (Y=0)	Bed end (Y=L)	
$u_{sfeed}C_{feed,i} = u_s C_{g,i} - \varepsilon D_z C_{gT} \frac{\partial y_i}{\partial z}$	$\frac{\partial y_i}{\partial z} = 0$	
$P = P_{feed} + (P_{srp} - P_{feed})e^{-k_p t}$	$u_s = 0$	
$u_{sfeed}C_{feed,T}C_P T_{feed} = u_s C_{gT} C_P T_g - \lambda \frac{\partial T_g}{\partial z}$	$\frac{\partial T_g}{\partial z} = 0$	